DOI: 10.3190/jgeosci.270

Appendix C

C1 Current and final velocity models

The next figures present the intermediate and final models obtained during the DRTG iterations along the S04, S02 and S03 profiles.

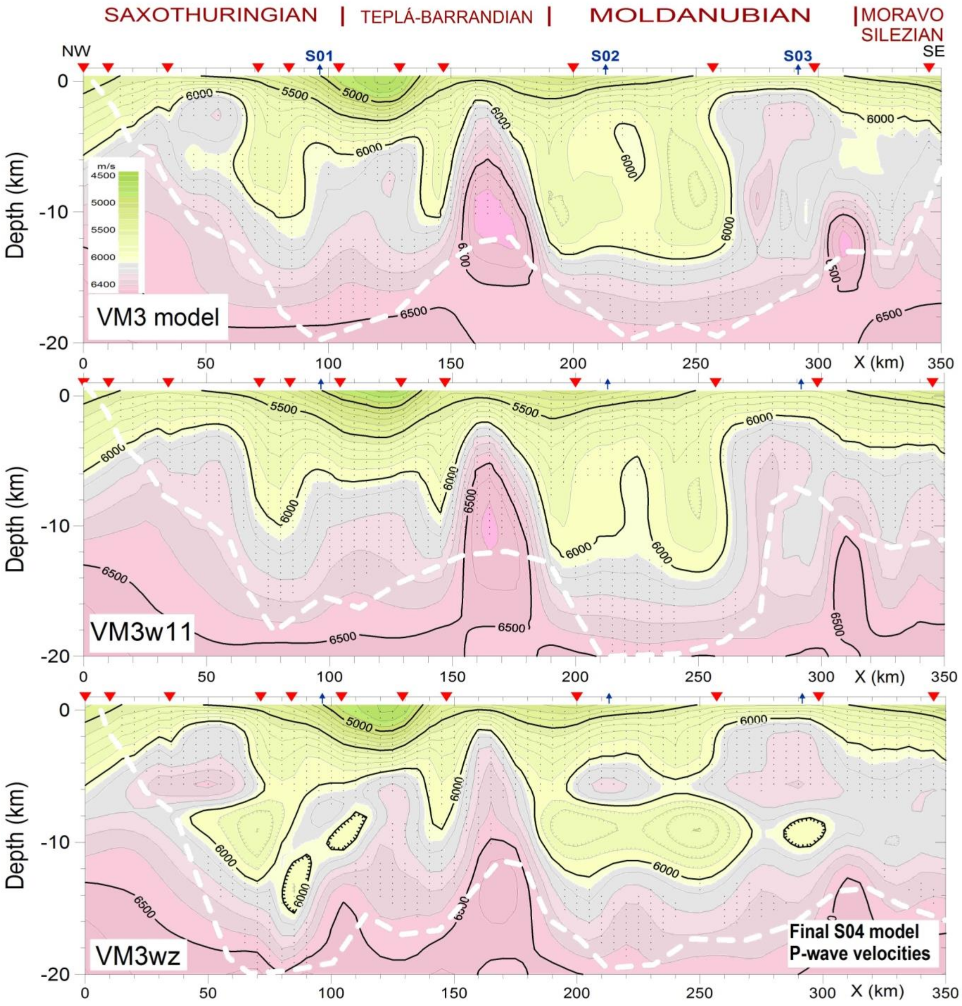

Fig. C1 The S04 models. (top) the VM3 model best-updated during the DRTG iterations; (middle) its smoothed version VM3w11 with the best ray coverage thanks to strongly reduced LVZ; (bottom) the final version VM3wz preserving LVZs in the 6–11 km depths. The verified model nodes are dotted. The verified parts of the models (marked by white borders) yielded the RMS fits of 132, 176 and 99 ms, respectively (Tab. 2).

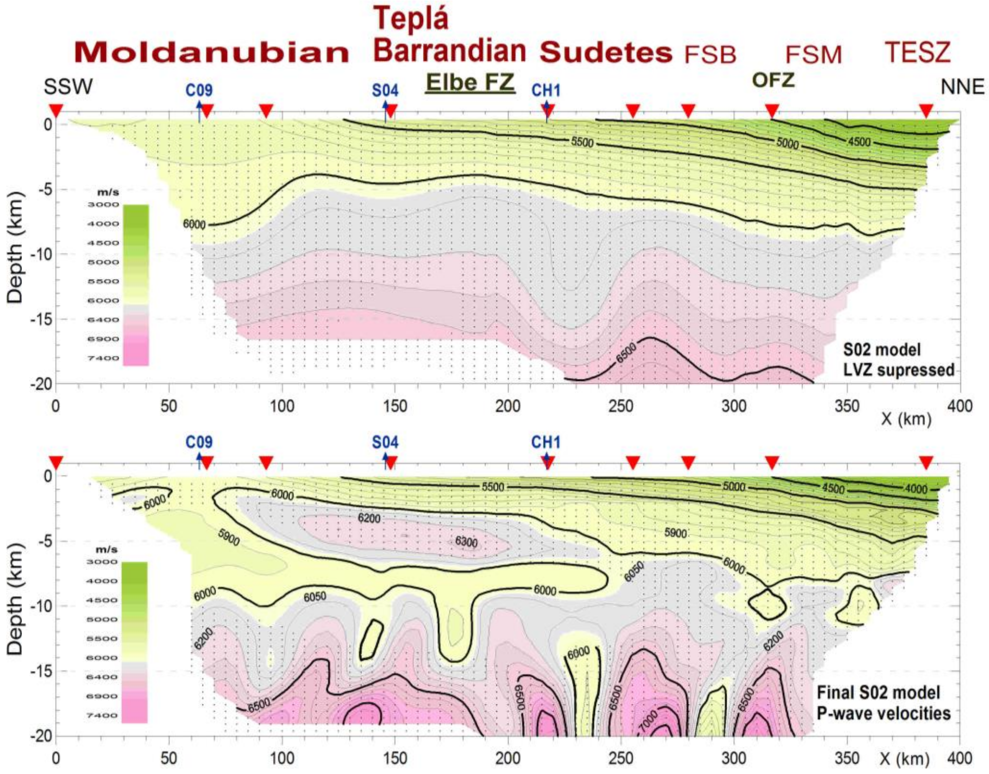

Fig. C2 The best-updated S02 model (top) and its final version preserving LV zones (bottom). Involving the LV zones improved the overall fit from 123 to 79 ms (Tab. 3). The verified model nodes are dotted. FZ – Fault Zone; OFZ – Odra Fault Zone; FSB – Fore-Sudetic Block; FSM – Fore-Sudetic Monocline; TESZ – Trans-European Suture Zone.

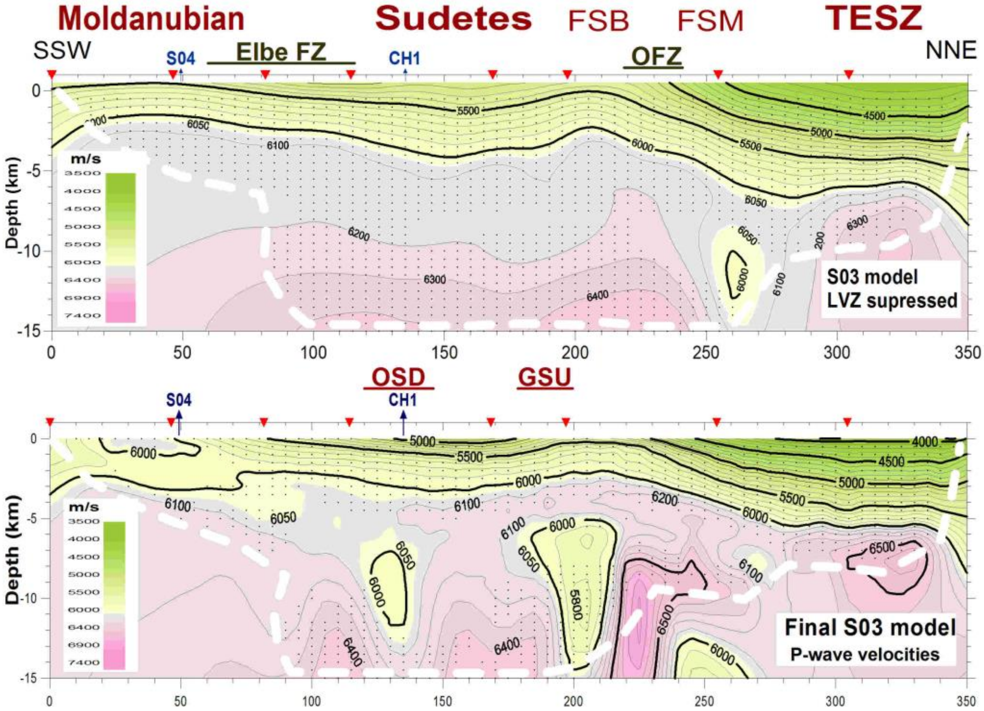

Fig. C3 The best-updated (top) and the final S03 model preserving LV zones (bottom). The verified model nodes are dotted. Involving the LV zones improved the overall fit from 153 to 68 ms (Tab. 3). FZ – Fault Zone; OFZ – Odra Fault Zone; FSB – Fore-Sudetic Block; FSM – Fore-Sudetic Monocline; TESZ – Trans-European Suture Zone; OSD – Orlica–Śnieżnik Dome; GSU – Góry Sowie Unit.

C2 Lateral resolution of extended velocity anomalies

The DRTG method provides the travel-time residuals $\{\Delta t(x,z)\}$ at single grid points fully characterizing the model fit achieved. They specify the standard deviations $\sigma(z)$ of the travel-time residuals $\{\Delta t(x,z)\}$ at single depth levels z. The target velocity anomalies ∂v_{an} cause the travel-time responses ∂t_{an} which the DRTG method can detect if they exceed the achieved travel-time residuals $\{\Delta t(x,z)\}$. The $\sigma(z)$ depth curves can then be used to assess which velocity anomalies can be yet resolved in a particular depth (Novotný 2011). A short recapitulation of basic equations for the statistical lateral resolution estimate follows.

Thanks to the prevailingly sub-horizontal spreading of refraction waves, the refraction tomographies are most sensitive to the lens-shaped velocity anomalies ∂v_{an} with the elongated lateral sizes L_{an}. Evidently, undistinguished remain those velocity anomalies ∂v_{an}, whose time responses ∂t_{an} do not exceed the travel-time residuals. In the case of negative anomalies forming the LV zones with no returns of refraction waves, the velocities inside these LV zones always remain inherently irresolvable (e.g., Aki and Richards 1980). The minimum lateral sizes of the "yet resolvable" anomalies can be derived as follows.

Consider a relatively weak velocity anomaly $|\partial v_{an}| << v$ with a lateral size L_{an}. It excites a time anomaly ∂t_{an} in the travel-times which can be expressed as $\partial t_{an} = \partial(L_{an}/v) = - L_{an}\partial v_{an}/v^2$ for a sub-horizontal spreading ray. Denoting its relative velocity excess as $r_{an}=\partial v_{an}/v$, L_{an} can be expressed as

$$L_{an}\left(z, r_{an}, \partial t_{an}\right) = -v\left(z\right)\partial t_{an} / r_{an} \, . \tag{C1}$$

The velocity anomalies $L_{an}(z,r_{an},\partial t_{an})$ will be resolved if their time responses ∂t_{an} emerge above the travel-time residuals. Assume that the normal distribution is valid for the time residuals $\{\Delta t(x_j,z)\}$. The 95% confidence level in resolving the L_{an} anomalies will then be achieved if their time responses $|\partial t_{an}|$ are equal to or greater than the doubled standard deviation, i.e., $|\partial t_{an}| \geq 2\sigma(z)$. Substituting it into (C1), one obtains

$$L_{an}(z, r_{an}, 2\sigma) = 2\sigma(z)v(z)/|r_{an}| . \tag{C2}$$

Similarly, requiring only $|\partial t_{an}| \geq \sigma(z)$, the limit size of the anomalies resolved with the lower 68% confidence can be expressed as

$$L_{an}(z, r_{an}, 1\sigma) = L_{an}(z, r_{an}, 2\sigma)/2 = \sigma(z)v(z)/|r_{an}| . \tag{C3}$$

As follows from (C3), a weaker (for instant 5%) velocity anomaly can attain the same confidence in resolution as the stronger (10%) one if it has the adequately larger size (twice).

The relation (C2) was used for calculation of the depth curves for the 10% velocity anomalies at 95% confidence level – see Figs 5, 7 and 8 in the main paper. Note that according to (C2), the lateral resolution of 10% anomalies at 95% confidence levels is the same as that due to the 5% anomalies at the lower 68% confidence level

$$L_{an}(z, 5\%, 1\sigma) = L_{an}(z, 10\%, 2\sigma) . \tag{C4}$$

The derivation is based on that the anomalous velocity bodies ∂v_{an} can be detected by refraction imaging if their time responses ∂t_{an} proportional to $L_{an}\partial v_{an}$ exceed the travel-time residuals. Therefore, to speak that a refraction tomography is able to determine local anomalies stronger than a certain value r_{an} is worthless until their sizes are not specified. For instant, a 1% velocity anomaly can be distiguished by the DRTG tomography (or any other) as well as the 5% one if its lateral size is 5 time larger.

C3 Comparison with the previous results

The derived DRTG models image the Earth's crust in the depth ranges of 20 km (the S04, S02, CEL09 profiles) or 15 km (the S03 profile) illuminated by the refraction waves. In these ranges, the previously published models can be compared with the DRTG results presented by Figs 9–12 in main paper.

Majdanski et al. (2006) processed the wide-angle data from the S02 and S03 profiles by three methods. For the derivation of P-wave velocities, the authors used two inverse methods, the pure refraction tomography (Hole 1992) and the JIVE3D optimization (Hobro 1999) combining both the reflected and refracted data. However, the final structural models, involving velocity and reflecting interfaces, were produced by the ray-tracing modeling (Majdanski et al. 2006, fig. 13). The velocity distributions, derived by the inverse methods, comprise several lateral anomalies, some extended over the entire crust thickness. Because of their unstable shapes generated by the methods applied, the authors evidently considered them as unreliable. No profound lateral velocity changes namely occur in their final velocity sections S02 and S03 except for the sedimentary cover (Majdanski et al. 2006, figs 5e and 6e). The shallow structures depicted from 8 to 24 km depths exhibit almost no lateral variations. In the 6–8 km depths, the S02 model shows a subtle LV inclusion (6000 m/s) extended from 130 to 300 km located beneath an isolated shorter HV anomaly (6100 m/s). This complex may correspond to the DRTG more pronounced shallow HV anomaly of 6100–6300 m/s and its underlying LV gradient-free zone with the velocities of 5900–6000 m/s (Fig. 10, km 80–220). Then, the lower velocity contrast and smaller extent of the compared complex may signalize a weaker performance in (Majdanski et al. 2006, fig. 5e). The DRTG imaging of the upper crust also show a steeper NNE dipping in the NNE ends of both S02 and

S03 sections growing toward the Trans-European Suture Zone (TESZ). Note that the NNE dips become steeper eastward in the S03 section behind the Odra fault zone (Figs 9–10).

Růžek et al. (2007) developed a special two-step approach suitable for a fast, non-iterative simultaneous inversion of refracted Pg, Pn and reflected PmP phases. The authors process the eight seismic profiles of the CELEBRATION 2000, ALP 2002 and SUDETES 2003 seismic experiments which cross the BM. First, using the differential evolution algorithm by Storn and Price (1997) the low-parametric initial velocity models with a fixed mantle–crust interface were derived. In the second step, these initial models were once refined by regularized tomographic corrections to satisfy the prescribed RMS travel-time residuals of ~100 ms. The S02, S03, S04 and CEL09 models, derived by (Růžek et al. 2007, figs 8–9), again show several velocity elevations and adjacent depressions extended across the entire crustal thickness. These major velocity features are compatible with those which Majdanski et al. (2006) obtained by the Hole’s inversion method – see their figs 5a and 6a. The crustal-scale S02 and S03 anomalies are more pronounced in (Růžek et al. 2007, Fig. 8). However, the shallow S02 anomalies discussed above were not resolved, perhaps owing to a rougher 3 km z-step used and just one iteration applied. Likely, for the same reasons, many minor features imaged by DRTG method (Figs 9–11) are missing in the S04, S02 and S03 sections derived by Růžek et al. (2007). The best agreement with the DRTG results concerns four major velocity elevations and adjacent depressions in the S04 section reaching the Moho depths (Růžek et al. 2007, fig. 9).

Hrubcová et al. (2005, 2010) used forward modeling based on the trial and error method to derive the S04 and CEL09 structural sections. The authors applied the ray tracing program package SEIS83 (Červený and Pšenčík 1984) provided by the interactive graphical interface (Komminaho 1997). As quoted, the S04 model (Hrubcová et al. 2010, fig. 5) fitted the input travel times within an accuracy of ± 200 ms for both refracted and reflected phases. The obtained multi-layers crustal models involve long sub-horizontal interfaces, which could only partly be confirmed by the wide-angle reflection modeling. If these models are compared with those obtained by Růžek et al. (2007), only a partial agreement can be seen for the depths less than ~5 km.

Geissler et al. (2012) studied the lithosphere structure of the NE Bohemian Massif. Using receiver function approach, they inferred the 1-D models based on the passive seismic data from the BOHEMA II experiment (Babuška et al. 2005) and also wide-angle data from the S02 shot-point No 42050 – see Tab. B1. Their analysis revealed additional Ps phases observed between 6 and 10 s delay time in the Sudetic region. The authors explained their origin by a mid-crustal LVZ between 16 and 20 km depth. They interpreted the LVZ as a felsic solidified magma reservoir of Permo–Carboniferous age located beneath the Sudetic Basins (see fig. 16 in Geissler et al. 2012). Searching for this LVZ in the previous S02 velocity models (Majdanski et al. 2006, fig. 5a; Růžek et al. 2007, fig. 8), a weak LVZ nearby the shot point 42050 occurs in both models. The LVZ, however, ranges shallower, between the 5 and 15 km depth. The S02 section derived by the DRTG method show two LV anomalies near the No 42050 shot-point (km 218, Fig. 10). Both reach the P-wave velocities lower than 6000 m/s. The former anomaly is an LV layer ranging from 5 to 10 km depth whereas the latter forms a diapir-like narrow LV body down to 20 km depth. Its depth range then corresponds to the felsic magma reservoir envisaged by Geissler et al. (2012). Near the No 42050 shot point, the S02 section crosses a 2D gravity modeling profile CH1 (Figs D1 and 1). The CH1 model (Chopin et al. 2012) shows lower densities in the 5–19 km depth interval which correspond to the decreased velocities at the crossing S02 section – see details in Appendix D.

References

AKI K, RICHARDS PG (1980) Quantitative Seismology, Volume II. W. H. Freeman and Company, San Francisco, pp 1–374

BABUŠKA V, PLOMEROVÁ J, VECSEY L, JEDLIČKA P, RŮŽEK B (2005) Ongoing passive seismic experiments unravel deep lithospheric structure of the Bohemian Massif. Stud Geophys Geod 49: 423–430

CHOPIN F, SCHULMANN K, SKRZYPEK E, LEHMANN J, DUJARDIN JR, MARTELAT JE, LEXA O, CORSINI M, EDEL JB, ŠTÍPSKÁ P, PITRA P (2012) Crustal influx, indentation, ductile thinning and gravity redistribution in a continental wedge: building a Moldanubian mantled gneiss dome with underthrust Saxothuringian material (European Variscan belt). Tectonics 31, doi: 10.1029/2011TC002951

ČERVENÝ V, PŠENČÍK I (1984) SEIS83 – Numerical modelling of seismic wave fields in 2-D laterally varying layered structures by the ray method. In: ENGDAL ER (ed) Documentation of Earthquake Algorithms. World Data Center A for Solid Earth Geophysics, Report SE–35. Boulder, Colorado, pp 36–40

GEISSLER WH, KÄMPF H, SKÁCELOVÁ Z, PLOMEROVÁ J, BABUŠKA V, KIND R (2012) Lithosphere structure of the NE Bohemian Massif (Sudetes) – a teleseismic receiver function study. Tectonophysics 564–565: 12–37

HOBRO JWD (1999) Three-Dimensional Tomographic Inversion of Combined Reflection and Refraction Seismic Travel-Time Data. Unpublished PhD Thesis, Department of Earth Sciences, University of Cambridge

HOLE JA (1992) Non-linear high-resolution three-dimensional seismic travel-time tomography. J Geophys Res 97: 6553–6562

HRUBCOVÁ P, ŚRODA P, ŠPIČÁK A, GUTERCH A, GRAD M, KELLER GR, BRUECKL E, THYBO H (2005) Crustal and uppermost mantle structure of the Bohemian Massif based on CELEBRATION 2000. J Geophys Res 110: B11305

HRUBCOVÁ P, ŚRODA P, GRAD M, GEISSLER WH, GUTERCH A, VOZÁR J, HEGEDÜS E, SUDETES 2003 WORKING GROUP (2010) From the Variscan to the Alpine Orogeny: crustal structure of the Bohemian Massif and the Western Carpathians in the light of the SUDETES 2003 seismic data. Geophys J Int 183: 611–633

KOMMINAHO K (1997) Software manual for programs MODEL and XRAYS – a graphical interface for SEIS83 program package. Department of Geophysics, University of Oulu, Oulu, Finland

MAJDANSKI M, GRAD M, GUTERCH A, SUDETES 2003 WORKING GROUP (2006) 2-D seismic tomographic and ray tracing modelling of the crustal structure across the Sudetes Mountains basing on SUDETES 2003 experiment data. Tectonophysics 413: 249–269

NOVOTNÝ M (2011) Depth-recursive tomography of Bohemian Massif at CEL09 transect – part A: deblurrring of velocity image and resolution estimates. Surv Geophys 32: 827–855

RŮŽEK B, HRUBCOVÁ P, NOVOTNÝ M, ŠPIČÁK A, KAROUSOVÁ O (2007) Inversion of travel times obtained during active seismic refraction experiments CELEBRATION 2000, ALP 2002 and SUDETES 2003. Stud Geophys Geod 51: 141–164

STORN R, PRICE K (1997) Differential evolution – a simple and efficient heuristic for global optimization over continuous spaces. J Glob Optim 11: 241–354